Self-trapped electrons and holes in PbBr2 crystals

AUTHOR(S):

Iwanaga, M; Azuma, J; Shirai, M; Tanaka, K; Hayashi, T

CITATION:

Iwanaga, M ...[et al]. Self-trapped electrons and holes in PbBr2 crystals. PHYSICAL REVIEW B 2002, 65(21): 214306.

ISSUE DATE:

2002-06-01

URL:

http://hdl.handle.net/2433/50225

PHYSICAL REVIEW B, VOLUME 65, 214306

Self-trapped electrons and holes in $PbBr_2$ crystals

Masanobu Iwanaga
Graduate School of Human and Environmental Studies, Kyoto University, Kyoto 606-8501, Japan

Junpei Azuma, Masanobu Shirai, and Koichiro Tanaka
Department of Physics, Graduate School of Science, Kyoto University, Kyoto 606-8502, Japan

Tetsusuke Hayashi
Faculty of Integrated Human Studies, Kyoto University, Kyoto 606-8501, Japan

(Received 15 January 2002; published 10 June 2002)

We have directly observed self-trapped electrons and holes in $PbBr_2$ crystals with the electron-spin-resonance (ESR) technique. The self-trapped states are induced below 8 K by two-photon interband excitation with pulsed 120-fs-width laser light at 3.10 eV. Spin-Hamiltonian analyses of the ESR signals have revealed that the self-trapping electron centers are the dimer molecules of Pb_2^{3+} along the crystallographic *a* axis and the self-trapping hole centers are those of Br_2^- with two possible configurations in the unit cell of the crystal. Thermal stability of the self-trapped electrons and holes suggests that both of them are related to the blue-green luminescence band at 2.55 eV coming from recombination of spatially separated electron-hole pairs.

DOI: 10.1103/PhysRevB.65.214306 PACS number(s): 71.20.Ps, 71.23.An, 71.38.Ht, 71.38.Mx

I. INTRODUCTION

Lead halide, $PbBr_2$ and $PbCl_2$, crystals decompose photochemically under ultraviolet (UV) light irradiation at room temperature.[1] At low temperatures, intense photoluminescence (PL) with a large Stokes shift is induced instead of the photochemical decomposition.[2,3] Because ionic conductivity is suppressed at low temperatures, it is thought that local lattice deformation just after photoexcitation does not induce further successive desorption of halogen ions and aggregation of lead ions. The local lattice deformation is most likely related to the PL at low temperatures. These phenomena imply the strong electron-phonon interaction in $PbBr_2$ and $PbCl_2$.

By studying the PL properties at low temperatures below 30 K in $PbBr_2$, it has been strongly suggested that bound- and free-electron-hole (e-h) pairs intrinsically relax into spatially separated pairs of a self-trapped electron (STEL) and a self-trapped hole (STH).[4,5] The relaxation probably results from the strong interaction of both electrons and holes with acoustic phonons.[6] To obtain further insight into the relaxation of e-h pairs, it is significant to investigate structurally the lattice-relaxed localized states with the electron-spin-resonance (ESR) technique in $PbBr_2$ photoirradiated below 30 K.

Structures of localized electronic states have been investigated so far in other ionic crystals. In x-ray irradiated crystals of alkali halides, ESR experiments have revealed that the holes localize on two nearest-neighbor halogen ions and form the dimer molecules of $(\text{halogen}_2)^-$ (Refs. 7 and 8). The top of the valence band is composed of the np states in X^- ions (X=F, Cl, and Br for n=2, 3, and 4, respectively), and the formation of the dimer-molecular STH is mainly attributed to the covalent bond of the np states.[9] On the other hand, holes in cubic PbF_2 irradiated with γ rays or neutrons localize on Pb^{2+} ions and form Pb^{3+} centers below 77 K.[10] Some calculations[11,12] for cubic PbF_2 have indicated that the top of valence band is mainly composed of the 6s states in Pb^{2+} ions. The STH structure is closely related to the valence-band structure. Moreover, Pb^{2+} ions can be effective hole traps and form Pb^{3+} centers in Pb-doped alkali halides.[13]

STEL's were first observed in $PbCl_2$ irradiated with x rays[14] or γ rays[15] at about 80 K; the STEL's form the dimer molecules of Pb_2^{3+} which are complementary to X_2^- (V_k center) in alkali halides, and the configuration is due to the conduction band composed of the 6p states in Pb^{2+} ions[12] and to the covalent bond of the 6p states. It was proposed that STH's in $PbCl_2$ form V_k-type Cl_2^- centers,[16] but the existence has been disputed. Although no definite experimental evidence simultaneously observing both STEL's and STH's has been reported so far, $PbCl_2$ and $PbBr_2$ are the candidates for yielding them.[17] The coexistence of STEL's and STH's gives evidence that both electrons and holes strongly interact with acoustic phonons,[6] and provides the experimental foundation for the further study of the uncommon relaxation including spontaneous e-h separation.[4,5,17]

In order to clarify the relaxed states of e-h pairs in $PbBr_2$, we have measured ESR signals induced with pulsed 120-fs-width and 3.10-eV laser light below 8 K. Spin-Hamiltonian analyses of the ESR signals have revealed that both electrons and holes get self-trapped, and, respectively, form dimer molecules of Pb_2^{3+} and Br_2^- as the self-trapping centers. We present the properties of ESR signals of $PbBr_2$ and the thermal stability in Sec. III, analyze the structures of the electron- and hole-trapping centers with spin Hamiltonians in Sec. IV, and discuss the correlation of STEL's and STH's with luminescence in Sec. V.

II. EXPERIMENTAL PROCEDURES

Single crystals of $PbBr_2$ were grown with the Bridgman technique from 99.999% powder purified under vacuum distillation. The crystal of orthorhombic D_{2h}^{16} (Refs. 18 and 19)

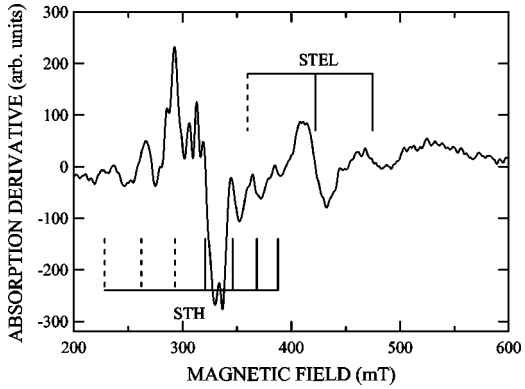

FIG. 1. Typical ESR spectrum measured at 5 K after photoirradiation at 5 K. Magnetic-field vector is in the ac plane and the direction corresponds to 65° in Fig. 3 below. Microwave frequency is 9.385 GHz. STEL and STH are described in Sec. III A. Solid lines indicate the prominent ESR positions. Dashed lines correspond to the ESR positions calculated from the spin Hamiltonian in Sec. IV.

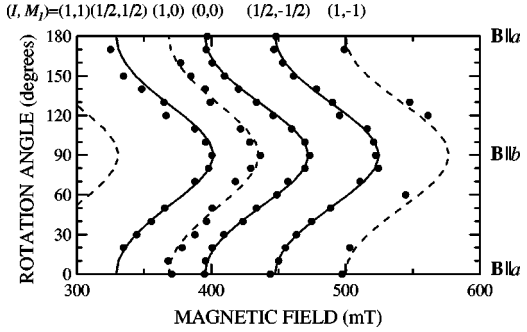

FIG. 2. Photoinduced STEL signals (closed circles) vs rotation angle measured at 8 K. Microwave frequency is 9.371(±0.001) GHz. Magnetic-field vector **B** is in the ab plane and the rotation axis is the c axis. (I,M_I): the total nuclear spin of the STEL centers and the magnetic quantum number. Solid and dashed lines: fitting lines derived from the spin Hamiltonian described in Sec. IV A.

was cut to a size of $3\times3\times3$ mm^3 along the right-angled crystallographic a,b, and c axes.

The crystal was sealed in a transparent quartz capillary with a transparent quartz rod and was fixed in a microwave cavity with a guide for light injection. The microwave cavity was a rectangular TE_{103}-mode cavity resonator with the quality factor $Q=3000$. The sample was photoirradiated below 8 K with second harmonics (pulsed 120-fs-width, 1-kHz, and 3.10-eV light) generated from a regeneratively amplified Ti:sapphire laser; the average power of the incident light was about 100 mW/cm^2 on the sample surface and the photoirradiation time was typically one hour. The incident photons induce the two-photon interband transition, create e-h pairs almost uniformly in the crystal, and produce measurable ESR signals within one minute. To avoid optical bleaching of the ESR signals, the sample after photoirradiation was kept dark during the measurement.

The photoirradiated sample was measured below 8 K with the ordinary ESR technique in the X-band range; the resonant microwave frequency was 9.378(±0.008) GHz. The rotation-angle dependence of the ESR signals was measured by rotating the crystal around the a, b, and c axes. Thermoluminescence (TL) under pulse annealing was measured through the transparent quartz rod attached to the sample. The total TL during the pulse annealing was directly detected by a photomultiplier, and the TL spectra at various pulse-annealing temperatures were measured with a charge-coupled device camera equipped with a grating monochromator. Raising and lowering rates of temperature under pulse annealing were about 5 K/s, and the sample was typically annealed for one second at each annealing temperature. The ESR spectra after pulse annealing were measured below 8 K.

III. EXPERIMENTAL RESULTS

A. Properties of ESR spectra

Figure 1 shows a typical ESR spectrum measured at 5 K after photoirradiation at 5 K. The solid lines in Fig. 1 indicate the prominent ESR positions and the dashed lines indicate the ESR positions calculated from the spin Hamiltonians in Sec. IV. The signals are classified into three groups by the rotation-angle dependence and the thermal profiles: (i) The ESR signals named STEL survive up to 130 K under pulse annealing. (ii) The signals named STH disappear under pulse annealing above 30 K. (iii) Though several signals at 280–340 mT cannot be well resolved because of the overlap with the STH signals, they survive above 100 K and almost disappear around 130 K under pulse annealing. The signals named STEL and STH, respectively, correspond to self-trapped electrons and holes, as analyzed in Secs. IV A and IV B.

ESR signals around 330 mT under UV light irradiation at 77 K were reported by several authors.[20–22] However, the ESR signals named STEL and STH have not been reported to our knowledge. Because of the overlap of the ESR signals, the spectrally well-resolved STEL and STH signals are mainly restricted to the region higher than 340 mT; in the region the intensity ratio of the STEL signals is 4:1 and that of the STH signals is 3:2:1. The STEL signals show linear response to the microwave power up to 10 mW even at 5 K. On the other hand, the STH signals saturate for microwave power higher than 0.01 mW at 6 K. The reduced linewidth of the STEL signals, $\Delta B=(g/g_0)\Delta B_0$, is estimated to be 14(±1) mT where g is the g value of the STEL, g_0 the free-electron g factor, and ΔB_0 the linewidth estimated from the experimental data; the ΔB is about three-times broader than $\Delta B=5.5$ mT in $PbCl_2$ (Ref. 14).

Figure 2 presents the rotation-angle dependence of the STEL signals (closed circles) at 8 K; magnetic-field vector **B** is in the ab plane and the rotation axis is the c axis. The index (I,M_I) denotes the pair of the total nuclear spin of the STEL center and the magnetic quantum number. The intensities of the ESR signals with indices (1,0) and (1,−1) are more than ten times as weak as that with (0,0). The intensity ratio between (0,0), (1/2,1/2), and (1/2,−1/2) is about 4:0.9:1. Solid and dashed lines fit the experimental data and are derived from the spin Hamiltonian (1) in Sec. IV A. A similar rotation-angle dependence of the STEL in $PbCl_2$ shows the twofold splits when **B** is in the bc and ac

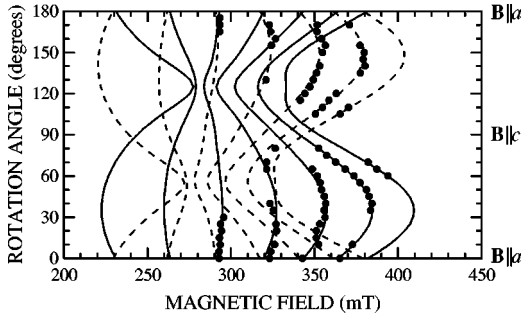

FIG. 3. Photoinduced STH signals (closed circles) vs rotation angle measured at 8 K. Microwave frequency is 9.383(±0.002) GHz. Magnetic-field vector **B** is in the *ac* plane and the rotation axis is the *b* axis. Solid and dashed lines: fitting lines derived from the spin Hamiltonian described in Sec. IV B.

planes;[14,15] the splits come from the two configurations reflecting the crystallographic symmetry. However, the explicit split has not been observed in $PbBr_2$ when **B** is in the *bc* and *ac* planes. Probably, the broad linewidth in $PbBr_2$ hides the split.

Figure 3 displays the rotation-angle dependence of the STH signals (closed circles); the magnetic-field vector **B** is in the *ac* plane and the rotation axis is the *b* axis. The signals are picked up from the ESR spectra as shown in Fig. 1. There exist the two series, each of which has more than three resonances. The two series are mirror symmetric for the *bc* plane with each other, reflecting the crystallographic mirror symmetry. Solid and dashed lines are derived from the spin Hamiltonian describing the hole center composed of two equivalent Br^- ions, and fit the STH signals.

B. Thermal stability of ESR signals and thermoluminescence

Figure 4 shows the thermal stability of the STH signals (closed circles) and the total TL intensity during the pulse annealing (open circles). The ESR signals after pulse annealing were measured at 6 K. The intensity of the STH signals sharply decreases above 20 K and the signals were hardly observed after pulse annealing at 40 K. The ESR signals at 280–340 mT also decrease up to 40 K by a similar amount

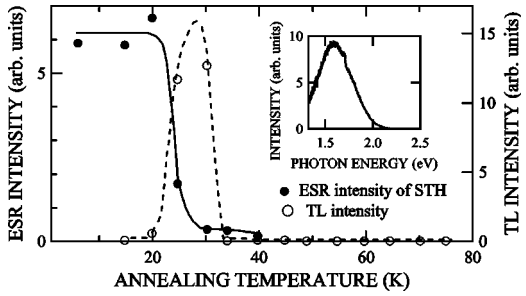

FIG. 4. ESR intensity of the STH signals (closed circles) and total TL intensity during pulse annealing (open circles). The abscissa stands for pulse-annealing temperature. The ESR signals after pulse annealing were measured at 6 K. Solid and dashed lines are guides for the eye. The inset displays the TL spectrum under pulse annealing at 22 K.

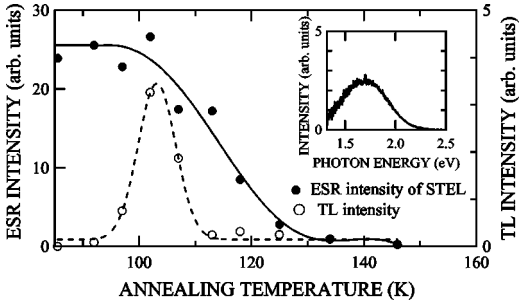

FIG. 5. ESR intensity of the STEL signals (closed circles) and total TL intensity during pulse annealing (open circles). The abscissa stands for pulse-annealing temperature. The ESR signals after pulse annealing were measured at 5 K. Solid and dashed lines are guides for the eye. The inset displays the TL spectrum measured around the peak of the TL curve (dashed line).

as the STH signals, and keep almost constant under pulse annealing at 40–100 K. TL appears corresponding to the quenching of the STH signals over 20–30 K. The TL spectrum under pulse annealing at 22 K is displayed in the inset of Fig. 4. The TL spectrum at 1.6 eV is spectrally in agreement with the red PL band; it is induced under excitation into the fundamental absorption region and increases 20–30 K instead of the decrease of the blue-green PL band at 2.55 eV.[4,5]

Figure 5 shows the thermal stability of the STEL signals (closed circles) and the total TL intensity during the pulse annealing (open circles). The ESR signals after pulse annealing were measured at 5 K. The intensity of the STEL signals decreases above 100 K and the signals are quenched at 145 K. The ESR signals at 280–340 mT also vanish together with the STEL signals. TL was observed over 90–140 K, strongly at 100–105 K. The TL spectrum measured around the peak of the TL curve is displayed in the inset of Fig. 5; the TL spectrum peaks at 1.7 eV and is located in the high-energy side in comparison with the spectrum in Fig. 4. The TL spectrum in Fig. 5 is spectrally in agreement with the PL spectrum in this temperature range. The PL has an extrinsic nature;[23] it is induced under excitation even in the energy range ($\hbar\omega \geqslant 3.5$ eV) lower than the fundamental absorption edge of 3.8 eV.[5]

IV. SPIN-HAMILTONIAN ANALYSIS

A. Structures of self-trapped electrons

The ESR signals prominently appearing at 410–530 mT have the *g* value of $g<2$ and therefore are ascribed to electron centers.[24] They have the similar rotation-angle dependence with each other as shown in Fig. 2, and thermally disappear together. The intensity ratio seems to reflect the isotope effect. Indeed, Pb^{2+} ions consist of nuclear spin $I=0$ (contained 79% naturally) and $I=1/2$ (contained 21% naturally). The pair of two equivalent Pb ions has the total nuclear spins of 0 (singlet), 1/2 (doublet), and 1 (triplet); the constituent ratio is 19.2:10:1. When the degeneracy of the multiplets is lifted, the ratio of the singlet to the two doublets

is 19.2:5:5≈4:1:1. This ratio is in agreement with the ratio 4:0.9:1 estimated from Figs. 1 and 2, and moreover it is probable that the far weak signals fitted with dashed lines in Fig. 2 come from the nondegenerate triplets.

Therefore, one can assume that an electron equivalently localizes on two nearest-neighbor Pb^{2+} ions and they form a Pb_2^{3+} center. The spin Hamiltonian $\mathcal{H}$ with Zeeman and hyperfine terms is given by

$$\mathcal{H}=\mu_B \mathbf{S}\cdot\underline{g}\cdot\mathbf{B}+g_0\mu_B\mathbf{I}_1\cdot\underline{A_1}\cdot\mathbf{S}+g_0\mu_B\mathbf{I}_2\cdot\underline{A_2}\cdot\mathbf{S}, \quad (1)$$

where μ_B denotes the Bohr magneton, $\mathbf{S}$ the electron spin, $\underline{g}$ the Zeeman tensor, $\mathbf{B}$ the magnetic-field vector, g_0 the free-electron g factor, $\mathbf{I}_i$ the nuclear spin, and A_i the hyperfine tensor $(i=1,2)$. The Pb-ion dimer does not contain the nuclear quadrupole term because $I_i=0$ or 1/2.

Each rotation-angle series of the ESR signals in Fig. 2 takes maximum and minimum values when $\mathbf{B}\|a$ and $\mathbf{B}\|b$. The dependence enables us to set the principal g and A axes such as $x=c$, $y=b$, and $z=a$.

Under axial symmetry $(A_x=A_y)$ and the second-order perturbation, taking the Zeeman term as the unperturbed term, the Hamiltonian (1) is transformed, as shown explicitly in Ref. 25, into the equation describing the allowed ESR transitions. The axial symmetry implies that the dimer-molecular axis is chosen to be the z axis.

The modified equation well describes the rotation-angle-dependent series of the ESR signals around the a,b, and c axes as in Fig. 2. The principal g values are obtained by fitting the Zeeman series of $I=0$; the solid line with index $(I,M_I)=(0,0)$ in Fig. 2 represents the fitted Zeeman line. Principal A values are obtained by fitting the series of $I=1/2$, using the principal g values; the solid lines with indices (1/2,1/2) and (1/2,−1/2) in Fig. 2 fit the series by varying the principal A values only. The dashed lines in Fig. 2 are drawn with the g and A values, and those with (1,0) and (1,−1) describe the series well. This analysis confirms that the ESR spectrum named STEL in Fig. 1 and the ESR signals in Fig. 2 originate from the electron-trapping center of Pb_2^{3+}. As for the electron centers, it is improbable that they are affected by vacancies or impurities because the rotation-angle dependence excludes the symmetry breaking around the electron centers by the permanent lattice defects. The coexistence of STEL's and ''perturbed'' STEL's by the defects is also excluded because of the single rotation-angle pattern and the thermal decay. Therefore, the electron centers named STEL in Fig. 1 are declared to be self-trapping electron centers of Pb_2^{3+}.

The structures of the STEL centers are schematically shown in Fig. 6; among the two nearest-neighbor Pb-ion pairs, the pairs along the a axis are the configurations consistent with the analysis unfolded in this section. In Fig. 6, each stick that bonds the two Pb^{2+} ions stands for the covalent bond via the localized electron. As described in Sec. III A, the broad linewidth of the STEL signals probably hides the twofold splits in the ab and ac planes observed in $PbCl_2$ (Refs. 14 and 15), and consequently the x and y axes determined here may deviate slightly from the principal x and y axes corresponding to each of the twofold splits.

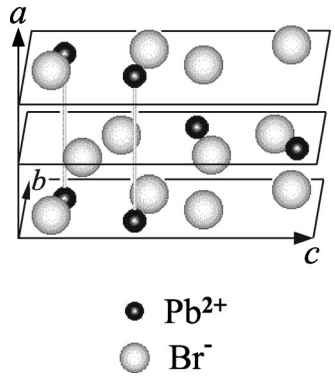

FIG. 6. Schematic configurations of the electron-self-trapping Pb_2^{3+} centers in $PbBr_2$ crystal. Four Pb^{2+} ions (small black balls) and eight Br^- ions (large white balls) in the two nearest-neighbor bc planes constitute the unit cell of the crystal. The lengths of the unit cell along the a, b, and c axes are 4.767, 8.068, and 9.466 Å, respectively (Ref. 18). There exist the two configurations of the STEL centers in the crystal, and each STEL center of Pb_2^{3+} is schematically represented with the two nearest-neighbor Pb^{2+} ions along the a axis and the stick that depicts the covalent bond of the two Pb^{2+} ions via the electron. The spin-Hamiltonian parameters of the Pb_2^{3+} center are listed in Table I.

The principal values of Zeeman g and hyperfine A tensors are listed in Table I. The principal g values vary from 1.4 to 1.7 and are comparable to the values of Pb_2^{3+} in $PbCl_2$ and NaCl:Pb.[14,15,26] This analysis only provides the absolute values of A_x, A_y, and A_z, and the principal A values are in the same order of several tens of mT as in $PbCl_2$ and NaCl:Pb. In accordance with Pb_2^{3+} in $PbCl_2$ and NaCl:Pb, the same signs of principal A values are chosen for Pb_2^{3+} in $PbBr_2$. The parameters ρ_s and A_σ of $PbBr_2$ are calculated with the g and A values in the perturbative analysis for the electronic levels of dimer-molecular centers.[9,26] The physical meanings of ρ_s and A_σ are discussed in Sec. V B.

B. Structures of self-trapped holes

The three prominent ESR signals at 350–390 mT named STH in Fig. 1 belong to the series with the similar rotation-angle dependence and the same thermal stability under pulse annealing. The intensity of the ESR signals at 280–340 mT decrease up to 40 K by a similar amount to the three signals at 350–390 mT. Therefore, there probably exist further signals at 280–340 mT of the same origin with the three signals at 350–390 mT, though the overlap with other signals prevents observing them separately. The ESR signals at 280–390 mT have the g values of $g\approx 2$ and probably originate from hole centers.[24]

In $PbBr_2$, we assume two equivalent nuclei Br_2^- as the hole center with more than three resonances at 280–390 mT. This assumption is consistent with the ratio of 3:2:1 estimated in Fig. 1; full signals of Br_2^- would be composed of seven resonances with the ratio of 1:2:3:4:3:2:1 in the first-order hyperfine effect associated with the Br-nuclear spin of 3/2.

The spin Hamiltonian $\mathcal{H}$ is also expressed by Eq. (1). For Br_2^-, a quadrupole term can be added as a second-order

TABLE I. Spin-Hamiltonian parameters of Pb_2^{3+} electron centers. Principal A_i values ($i=x,y,z$), ρ_s, and A_σ are represented in mT. The meanings of ρ_s and A_σ are discussed in Sec. V B. The parameters of Pb_2^{3+} centers in $PbCl_2$ and NaCl:Pb are also cited for comparison.

Electron center	g_x	g_y	g_z	A_x	A_y	A_z	ρ_s	A_σ
Pb_2^{3+} in $PbBr_2$[a]	1.563 ±0.002	1.416 ±0.002	1.690 ±0.002	−87 ±4	−87 ±3	100 ±5	39	−14
Pb_2^{3+} in $PbCl_2$[b]	1.549 ±0.001	1.379 ±0.001	1.718 ±0.003	−85 ±1	−85 ±1	109 ±1	39	−5
Pb_2^{3+} in $PbCl_2$[d]	1.494 ±0.005	1.322 ±0.005	1.662 ±0.005	NR[c]	NR	NR	NR	NR
Pb_2^{3+} in NaCl:Pb[e]	1.469 ±0.002	1.300 ±0.002	1.621 ±0.002	−115 ±1	−123 ±1	115 ±1	46	−29

[a]This work; Sec. IV A.
[b]Reference 14.
[c]Not reported (NR).
[d]Reference 15.
[e]References 14 and 26.

effect[25] because the nuclear spin of Br^- is 3/2. However, explicit second-order effects have not been observed in our measurements. Therefore, we apply Eq. (1) containing only the first-order term to the experimental data and moreover hypothesize the agreement of principal g and A axes.

As shown in Fig. 3, the solid-line and dashed-line series are mirror symmetric for the bc plane, and the rotation-angle dependence implies that the principal g and A axes deeply tilt from any crystallographic axis. This deviation and the overlap of the signals at 280–340 mT make it difficult to determine the orientation of principal x, y, and z axes. However, it is possible only to determine approximately the orientation of the z axis from the well-resolved signals at 350–390 mT. Thus, the first and second Euler angles are, respectively, 51° and 126° for the series fitted with the solid lines in Fig. 3, and 129° and 126° for the dashed lines. The third angle cannot be determined experimentally. We assume the angle to be 0°, and consequently the orientation of x and y axes determined here is not necessarily in agreement with the principal x and y axes of Br_2^- centers. The spin-Hamiltonian analysis is performed in a similar procedure as that described in Sec. IV A, except for $I=3$. As shown in Fig. 3, the Hamiltonian well describes the rotation-angle dependence of the three prominent signals at 350–390 mT and some other prominent signals in the region lower than 340 mT. Table II presents the principal g and A values obtained by the fitting and shows that the values of Br_2^- centers in $PbBr_2$ are comparable to those in alkali bromides. Though this spin-Hamiltonian analysis cannot provide the signs of hyperfine parameters A_x, A_y, and A_z, the molecular analysis[9] of electronic levels in Br_2^- centers requires the signs to be positive, and the same signs are chosen in $PbBr_2$ in accordance with the analysis. The parameters ρ_s and A_σ in Table II are discussed in comparison with those of other host crystals in Sec. V B.

The Br-ion pairs whose axis is in agreement with the principal z axis of the solid-line series in Fig. 3 are limited to pair a in Fig. 7; for pair a, the first and second Euler angles of the molecular axis are, respectively, 50.7° and 126.1° when the

TABLE II. Spin-Hamiltonian parameters of Br_2^- hole centers. Principal $A_i(i=x,y,z)$ values, ρ_s, and A_σ are represented in mT. The meanings of ρ_s and A_σ are discussed in Sec. V B. The parameters of Br_2^- centers in KBr, NaBr, and RbBr are cited for comparison.

Hole center	g_x	g_y	g_z	A_x	A_y	A_z	ρ_s	A_σ
Br_2^- (pair a)[a] in $PbBr_2$	2.16 ±0.02	2.17 ±0.02	1.90 ±0.01	10 ±4	10 ±4	46 ±1	16	17
Br_2^- (pair b)[a] in $PbBr_2$	2.18 ±0.05	2.23 ±0.05	1.90 ±0.03	10 ±1	10 ±1	46 ±7	19	14
Br_2^- in NaBr[b]	2.1514	2.1968	1.9791	6.50	7.38	43.1	18.23	12.66
Br_2^- in KBr[b]	2.1629	2.1623	1.9839	7.68	7.66	45.0	17.98	14.45
Br_2^- in RbBr[b]	2.1683	2.1524	1.9846	8.36	8.12	45.5	17.80	15.13

[a]This work; Sec. IV B.
[b]Reference 9; the accuracies of parameters g and A are within ±0.0005 and ±0.07, respectively.

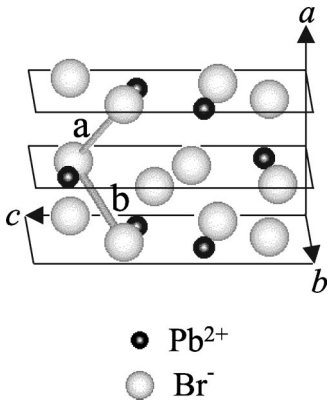

FIG. 7. Schematic configurations of the hole-self-trapping Br_2^- centers in $PbBr_2$ crystal. Br_2^- is composed of two Br^- ions (large white balls) and one hole. Each stick schematically represents the covalent bonds of two Br^- ions via the hole. The two dimer-molecular Br_2^-, named a and b, respectively, correspond to the solid-line and dashed-line series in Fig. 3. Two Pb^{2+} ions (small black balls) and four Br^- ions are sited in each bc plane. The spin-Hamiltonian parameters of the Br_2^- centers (pairs a and b) are listed in Table II.

lattice ions are located at the equilibrium positions. Similarly, the dashed-line series in Fig. 3 corresponds to pair b in Fig. 7; the first and second Euler angles are 129.3° and 126.1°, respectively. Pairs a and b are indeed mirror symmetric for the bc plane.

The good agreement of the dimer-molecular axes with the direction of the Br-ion pairs in the crystal confirms that the STH signals originate from the Br_2^- centers which are not affected by any permanent lattice defect. Therefore, the hole centers named STH in Sec. III A are ascribed to the self-trapping hole centers of Br_2^-.

V. DISCUSSION

A. Correlation of self-trapped states with luminescence

Thermal stability of the ESR signals indicates that the STEL's and the STH's coexist only in the temperature range below 30 K. Therefore, intrinsic luminescence related to both STEL's and STH's would appear below 30 K.

The blue-green (BG) PL band at 2.55 eV is the dominant intrinsic PL below 20 K in $PbBr_2$, and the phosphorescent decay is well described by the radiative recombination model.[5] The model assumes the process whereby the spatially separated e-h pair gets close by tunneling motion, forms a self-trapped exciton (STE), and recombines with radiation. The phosphorescent decay suggests that the BG-PL band originates from the distant pairs of a STEL and a STH.

The BG-PL band thermally decreases at 20–30 K and disappears above 30 K.[5] The thermally stable range of the BG-PL band corresponds to that of both STEL's and STH's. This correspondence supports the fact that the BG-PL band is closely related to both STEL's and STH's. In particular, the BG-PL band is not induced in the temperature range above 30 K, where the STH's disappear as shown in Fig. 4. Therefore, it is plausible that the STE's yielding the BG-PL have the configuration of (Br_2^- + electron), though it is unknown whether the STE is the nearest-neighbor pair of a STH and a STEL or whether it has the configuration in which a Br_2^- center bounds an electron in the excited orbital. On the other hand, the red PL band grows instead of the quenching of the BG-PL band at 20–30 K; as shown in Fig. 4, the temperature range corresponds to the growth of the red TL that has the same shape as the red PL band. Because of the instability of the STH centers at 20–30 K, the red PL and the red TL are ascribed to the STE's associated with the STEL centers of Pb_2^{3+} stable at 20–30 K. To clarify the configurations of the self-trapped excitons directly, the examination with an optically detected magnetic-resonance technique is preferable, because this ESR study can only suggest the configurations of the STE's yielding the BG-PL and the red PL bands.

As for the thermal stability of self-trapping centers, it is to be noted that the temperature at which the STH's and the STEL's disappear under pulse annealing does not necessarily indicate that of the thermal quenching of the self-trapping centers themselves. Indeed, the thermal decay of Br_2^- in alkali halides is affected by the thermal activation of trapped electrons and positive vacancies.[9] In $PbBr_2$, vacancies of Br^- and Pb^{2+} ions inevitably exist because of the high ionic conductivity,[27,28] and the density of Br^- vacancy is estimated at more than 10^{17} cm^{-3}. Consequently, it is likely that the thermal activation of vacancies affects the STH's: (i) it makes the self-trapped states unstable, induces the thermal transfer of the holes, and leads the holes to radiative and/or nonradiative decay, or (ii) it deforms the self-trapping centers to other trapping centers associated with vacancies. The thermal stability of the STEL's may be also affected by the thermal activation of other hole centers as discussed in Sec. V C.

B. Electronic structures of self-trapping centers

In this section we tentatively apply the perturbative analysis of Refs. 9 and 26 to the dimer centers, and discuss the electronic structures of STEL's and STH's in $PbBr_2$ from the comparison with other crystals. According to the analysis,[26,9] the mixing by spin-orbit interaction between the ground σ_g and excited orbitals π_g^x, π_g^y in the dimer molecule of Pb_2^{3+} and Br_2^- are calculated from the g shift and the principal A values under the Hartree-Fock approximation and the second-order perturbation taking the spin-orbit interaction as the perturbed term. The parameters ρ_s in Tables I and II denote the dipole-dipole interaction between the magnetic moments of the electron (or hole) and nuclei, and represent the anisotropic contribution to the hyperfine term. The parameters A_σ represent the isotropic contribution to the A tensor and are given by $A_\sigma = A_\sigma^s + A_\sigma^e$ where A_σ^s is the positive Fermi contact term and A_σ^e the negative exchange-polarization term of the inner electrons.

For Pb_2^{3+}, A_σ^s is proportional to $6s$-state mixing into the ground orbital $\sigma_g = \alpha_g(6s_1 + 6s_2) + \beta_g(6p_{1,z} - 6p_{2,z})$ where α_g and β_g are constants, and $6s$ and $6p$, respectively, denote the atomic wave functions of the $6s$ and $6p$ states in Pb^{2+}. ρ_s is $\rho_s \propto \beta_g^2 \langle r^{-3} \rangle$ where $\langle r^{-3} \rangle$ is the spatial distribution of

the electron, and the small ρ_s values result in the spread of the electron as long as the β_g's of Pb_2^{3+} are comparable in different host crystals. As shown in Table I, ρ_s in $PbBr_2$ has the same value as that in $PbCl_2$ and is 15% smaller than that in NaCl:Pb; the ρ_s suggests that the distribution of STEL in $PbBr_2$ spreads as outwardly as in $PbCl_2$ and more outwardly than in NaCl:Pb. A_σ in $PbBr_2$ is negatively 2.8 times larger than that in $PbCl_2$. In other words, the positive part A_σ^s, which reflects $6s$ mixing into the ground orbital σ_g, contributes more than the negative A_σ^e in $PbCl_2$. This result qualitatively suggests that $6s$ mixing into the σ_g is larger in $PbCl_2$ than in $PbBr_2$. The difference is probably ascribed to the components of the top of valence band. The valence-band structure of $PbCl_2$ with more mixing of $6s$ states in Pb^{2+} ions may make it possible for the holes to form STH centers of Pb^{3+} as observed in PbF_2 (Ref. 10). Indeed, the mixing ratios of the $6s$ states into the top of the valence bands become large in order of $PbBr_2$, $PbCl_2$, and PbF_2 (Ref. 12).

The complementary discussion can be applied to Br_2^-. Parameters ρ_s and A_σ in Table II are comparable to each other. This analysis implies that the distribution of STH and the orbital functions of the σ_g in $PbBr_2$ are quite similar to those in alkali bromides.

C. Other trapping centers associated with lattice defects

The ESR signals at 280–340 mT have the g values of $g \geqslant 2$, and the overlap of the signals prevents discriminating each signal and analyzing with a spin Hamiltonian. However, they vanish together with the STEL signals around 120 K under pulse annealing, and then the crystal emits TL as shown in Fig. 5. Therefore, the signals at 280–340 mT are most likely to originate from hole-trapping centers.

From the valence-band structure, the Pb^{3+} center can be considered as another candidate for the intrinsic hole-trapping center, but the satellites, which stem from the isotope ^{207}Pb of $I=1/2$ (contained 21% naturally), have not been observed at 0–1 T just as seen in PbF_2 crystals[10] and Pb-doped KCl crystals.[13] Interstitial lattice defects, namely, Frenkel defects have been also excluded in $PbBr_2$.[27,28] Consequently, the signals at 280–340 mT except for the unresolved STH signals probably originate from the extrinsic hole center associated with the permanent lattice defects such as vacancy, impurity, or both. The extrinsic hole-trapping centers are efficient competitors of the STH centers because they survive above 100 K together with not a few STEL and disappear around 120 K with emitting TL.

VI. CONCLUSIONS

Self-trapping electron and hole centers are simultaneously photoinduced by two-photon interband excitation with 120-fs-width laser light at 3.10 eV and have been directly detected with the ESR technique. The excitation enables us to induce e-h pairs with enough density for the present ESR measurements. Spin-Hamiltonian analyses have revealed that the structures of STEL's and STH's are the dimer-molecular Pb_2^{3+} and Br_2^-, respectively. The STEL centers of Pb_2^{3+} orient along the crystallographic a axis. The holes select self-trapping sites among many nearest-neighbor Br-ion pairs in the unit cell, and form the STH centers of Br_2^- with the two particular orientations. From the comparison of the principal g and A values, the Pb_2^{3+} and the Br_2^- centers are similar to those in other crystals studied so far.

From this ESR study, we conclude that both electrons and holes in $PbBr_2$ crystals strongly interact with acoustic phonons and do relax into the individual self-trapped states. Moreover, the STEL's and the STH's centers coexist below 30 K, and the STH centers disappear at 20–30 K. The temperature range is in good agreement with the range in which the phosphorescent blue-green PL band at 2.55 eV is induced. The agreement supports the conclusion of the previous PL study (Ref. 5) that both STEL and STH centers are related to the radiative recombination process yielding the blue-green PL band.

[1] J.F. Verwey, J. Phys. Chem. Solids **31**, 163 (1970).
[2] W.C. De Gruijter and T. Bokx, J. Solid State Chem. **6**, 271 (1973).
[3] G. Liidja and Vl. Plekhanov, J. Lumin. **6**, 71 (1973).
[4] M. Iwanaga, M. Watanabe, and T. Hayashi, J. Lumin. **87-89**, 287 (2000).
[5] M. Iwanaga, M. Watanabe, and T. Hayashi, Phys. Rev. B **62**, 10 766 (2000).
[6] A. Sumi, J. Phys. Soc. Jpn. **43**, 1286 (1977).
[7] K.S. Song and R.T. Williams, *Self-Trapped Excitons* (Springer, Berlin, 1993).
[8] R.H. Silsbee, in *Electron Paramagnetic Resonance*, edited by S. Geschwind (Plenum, New York, 1972), Chap. 7.
[9] D. Schoemaker, Phys. Rev. B **7**, 786 (1973).
[10] M. Nishi, H. Hara, Y. Ueda, and Y. Kazumata, J. Phys. Soc. Jpn. **42**, 1900 (1977).
[11] M. Nizam, Y. Bouteiller, B. Silvl, C. Pisani, M. Causa, and R. Dovesi, J. Phys. C **21**, 5351 (1988).
[12] M. Fujita, M. Itoh, Y. Bokumoto, H. Nakagawa, D.L. Alov, and M. Kitaura, Phys. Rev. B **61**, 15 731 (2000).
[13] D. Schoemaker and J.L. Kolopus, Solid State Commun. **8**, 435 (1970).
[14] S.V. Nistor, E. Goovaerts, and D. Schoemaker, Phys. Rev. B **48**, 9575 (1993).
[15] T. Hirota, T. Fujita, and Y. Kazumata, Jpn. J. Appl. Phys., Part 1 **32**, 4674 (1993).
[16] S.V. Nistor, E. Goovaerts, M. Stefan, and D. Schoemaker, Nucl. Instrum. Methods Phys. Res. B **141**, 538 (1998).
[17] M. Iwanaga, M. Watanabe, and T. Hayashi, Int. J. Mod. Phys. B **15**, 3677 (2001).
[18] R.W.G. Wyckoff, *Crystal Structures*, 2nd ed. (Wiley, New York, 1963), Vol. 1.
[19] A.F. Wells, *Structural Inorganic Chemistry*, 5th ed. (Clarendon, Oxford, 1984), p. 273.

[20] J. Arends and J.F. Verwey, Phys. Status Solidi **23**, 137 (1967).
[21] W.C. De Gruijter and J. Kerssen, J. Solid State Chem. **5**, 467 (1972).
[22] J. Kerssen, W.C. De Gruijter, and J. Volger, Physica (Amsterdam) **70**, 375 (1973).
[23] M. Iwanaga (unpublished).
[24] C.P. Slichter, *Principals of Magnetic Resonance*, 3rd ed. (Springer, Berlin, 1990), Chap. 11.
[25] D. Schoemaker, Phys. Rev. **174**, 1060 (1968).
[26] I. Heynderickx, E. Goovaerts, and D. Schoemaker, Phys. Rev. B **36**, 1843 (1987).
[27] J.F. Verwey and J. Schoonman, Physica (Amsterdam) **35**, 386 (1967).
[28] J. Oberschmidt and D. Lazarus, Phys. Rev. B **21**, 5813 (1980).